Cs₃Bi₂Br₉ nanoparticles decorated C₃N₄ nanotubes composite photocatalyst for highly selective oxidation of benzylic alcohol

Yang Ding[a,b,†], Chunhua Wang[c,d,†]*, Sateesh Bandaru[a], Lang Pei[a], Runtian Zheng[b], Yun Hau Ng[d], Daniel Arenas Esteban[e], Sara Bals[e], Jiasong Zhong[a]*, Johan Hofkens[c], Gustaaf Van Tendeloo[e], Maarten B. J. Roeffaers[f], Li-Hua Chen[g]* and Bao-Lian Su[b,g]*

[a] College of Materials and Environmental Engineering, Hangzhou Dianzi University, Hangzhou 310018, China.

[b] Laboratory of Inorganic Materials Chemistry (CMI), University of Namur, 61 rue de Bruxelles, B-5000, Namur, Belgium.

[c] Department of Chemistry, KU Leuven, Celestijnenlaan 200F, B-3001 Leuven, Belgium.

[d] School of Energy and Environment, City University of Hong Kong, 83 Tat Chee Avenue, Kowloon, Hong Kong, China.

[e] Electron Microscopy for Materials Science (EMAT), University of Antwerp, 2020 Antwerp, Belgium.

[f] cMACS, Department of Microbial and Molecular Systems, KU Leuven, Celestijnenlaan 200F, Leuven 3001, Belgium.

[g] State Key Laboratory of Advanced Technology for Materials Synthesis and Processing, Wuhan University of Technology, 122, Luoshi Road, 430070 Wuhan, Hubei, China.

*Corresponding authors: chunhua.wang@cityu.edu.hk, jiasongzhong@hdu.edu.cn, chenlihua@whut.edu.cn, bao-lian.su@unamur.be.

[†]Y. Ding and C. Wang contributed equally to this work.

Abstract

Solar-light driven oxidation of benzylic alcohols over photocatalysts endows significant prospects in value-added organics evolution owing to its facile, inexpensive and sustainable process. However, the unsatisfactory performance of actual photocatalysts due to the inefficient charge separation, low photoredox potential and sluggish surface reaction impedes the practical application of this process. Herein, we developed an innovative Z-Scheme Cs₃BiBr₉ nanoparticles@porous C₃N₄ tubes (CBB-NP@P-tube-CN) heterojunction photocatalyst for highly selective benzyl alcohol oxidation. Such composite

1

combining increased photo-oxidation potential, Z-Scheme charge migration route as well as the structural advantages of porous tubular C_3N_4 ensures the accelerated mass and ions diffusion kinetics, the fast photoinduced carriers dissociation and sufficient photoredox potentials. The CBB-NP@P-tube-CN photocatalyst demonstrates an exceptional performance for selective photo-oxidation of benzylic alcohol into benzaldehyde with 19, 14 and 3 times higher benzylic alcohols conversion rate than those of C_3N_4 nanotubes, $Cs_3Bi_2Br_9$ and $Cs_3Bi_2Br_9$@bulk C_3N_4 photocatalysts, respectively. This work offers a sustainable photocatalytic system based on lead-free halide perovskite toward large scale solar-light driven value-added chemicals production.

Keywords: photo-oxidation, porous nanotubes, $Cs_3Bi_2Br_9$, benzylic alcohols, Z-Scheme

1. Introduction

Benzaldehyde as an important chemical product is widely used in flavor, fragrance and pharmaceutical industry [1-3]. So far, the conventional organic synthesis route with high temperature and pressure as well as long reaction time has been predominantly adopted for the preparation of benzaldehyde [4]. Recently, the production of benzaldehyde via a solar light driven synthesis has aroused numerous interest owing to its facile, green, energy-saving and sustainable characteristics [5-8]. Light driven benzyl alcohol conversion into benzaldehyde using oxygen as reactant with water as the single by-product is a significantly promising sustainable process [9-12]. However, unsatisfactory activity and selectivity impede the practical application of light driven benzyl alcohol conversion [13]. Thus, the exploration of high performance photocatalyst is extremely urgent.

Halide perovskite materials with an ABX_3 structure have appealed significant attention owing to their potential applications in LEDs, solar cells and energy conversion devices [14-17]. These materials possess attractive characteristics such as high extinction coefficients, excellent light response ability and tunable electronic configurations, being well matched with the demand for highly efficient

photocatalysts [18-20]. For instance, $Cs_3Bi_2Br_9$ photocatalyst demonstrated better performance for photocatalytic dye degradation than that of traditional CdS photocatalyst [21]. Moreover, a variety of halide perovskites such as $CsPbBr_3$, $Cs_2AgBiBr_6$ etc. were explored for efficient photoreduction of CO_2 [22-24]. However, the relatively narrow band gap (< 2.8 eV) results in the unsatisfactory photoredox ability of perovskite materials, thus limiting their photocatalytic applications and activity [25]. Combining with other semiconductors to generate heterostructure with enough photoredox potential is considered as an effective strategy [21,22]. Graphitic carbon nitride (g-C_3N_4) has attracted tremendous interest in photocatalytic fields such as water splitting, CO_2 reduction, and organics conversion [26-30]. The structure of g-C_3N_4 exerts a significant effect on its physicochemical characteristics and therefore influences its photocatalytic performances [31-33]. So far, various morphologies of g-C_3N_4 photocatalysts like nanosheets, nanorods, and nanotubes have been explored. Among these, one-dimensional (1D) g-C_3N_4 structures have shown outstanding properties of 1D configuration in facilitating the electron transfer kinetics [34-36]. Coupling the merits of high photocatalytic potential of perovskite materials and desirable structure of 1D g-C_3N_4 could be a promising solution for improved photocatalytic value-added chemicals evolution. So far, rare studies have been conducted in this direction.

Herein, we developed an innovative Z-Scheme $Cs_3Bi_2Br_9$ nanoparticles@highly porous C_3N_4 nanotubes (CBB-NP@P-tube-CN) heterojunction photocatalyst. Such material can harmonize the synergistic effects of enhanced light harvesting, facile mass diffusion and electrons transfer as well as increased photo-oxidation potential. The photocatalytic activity of the hybrid composite for direct one-step selective photo-oxidation of benzylic alcohol into benzaldehyde shows about 19, 14 and 3 times higher than that of pure C_3N_4 nanotubes, $Cs_3Bi_2Br_9$ and $Cs_3Bi_2Br_9$@bulk C_3N_4 photocatalysts, respectively. The Z-Scheme CBB-NP@P-tube-CN heterojunction with beneficial hierarchical porous structure and enhanced photoredox ability can maximize the photocatalytic performance for a step forward to realizing large scale solar-light driven value-added chemicals production.

2. Experimental section

2.1 Materials

Cesium bromide (CsBr, 99.9%), Bismuth(III) bromide (BiBr$_3$, 99.9%), benzyl alcohol (C$_6$H$_5$OH, 99.9%), and Dimethyl sulfoxide (DMSO, 99.9%) were purchased from Sigma-Aldrich. Benzotrifluoride (BTF, 99.9%) was purchased from Alfa Aesar. Melamine was supplied by Aladdin Co., Ltd. All chemicals were used without further purification.

2.2 Synthesis of bulk g-C$_3$N$_4$ (bulk-CN), and porous C$_3$N$_4$ nanotubes (P-tube-CN)

B-CN was synthesized by direct calcination of melamine powder in a muffle furnace at 550 °C for 4 h. For the synthesis of P-tube-CN, 1 g melamine powder is dissolved in 50 mL of deionized water under magnetic stirring at 80 °C for 30 min and a clear solution is obtained. Subsequently the as-prepared melamine solution is transferred into a 50 mL Teflon stainless autoclave with a hydrothermal treatment at 180 °C for 24 h in an oven. The obtained super-molecular nanorods are further calcinated at 550 °C for 4 h under Air atmosphere. After cooling to room temperature, the tube-CN powder is finally prepared.

2.3 Preparation of Cs$_3$Bi$_2$Br$_9$ material

Cs$_3$Bi$_2$Br$_9$ was synthesized using an anti-solvent precipitation method at room temperature. First, CsBr and BiBr$_3$ with a mole ratio of CsBr:BiBr$_3$=3:2 was dissolved in dimethyl sulfoxide (DMSO) to prepare a 0.3 M Cs$_3$Bi$_2$Br$_9$ precursor solution. Second, the Cs$_3$Bi$_2$Br$_9$ precursor solution was added to isopropanol and the Cs$_3$Bi$_2$Br$_9$ suspension was collected by centrifugation. Finally, the Cs$_3$Bi$_2$Br$_9$ powder was dried in a vacuum oven at 70 °C overnight.

2.4 Synthesis of CBB-NP@P-tube-CN composite

A series of x wt% Cs$_3$Bi$_2$Br$_9$@C$_3$N$_4$ photocatalysts were synthesized via an in-situ synthesis method. In a typical experiment, Cs$_3$Bi$_2$Br$_9$ precursor solution containing 15 mg of Cs$_3$Bi$_2$Br$_9$ was added to 85 mg C$_3$N$_4$ nanotubes, followed by vigorously stirring for 2 h at room temperature. Then, the 15% CBB-NP@P-tube-CN hybrid was first heated at 95 °C for 1 h in a glovebox and dried at 80 °C in a vacuum oven for 12 h.

2.5 Characterizations

X-ray diffraction (XRD) patterns were obtained on a Bruker D8 system with Cu Ka radiation (λ = 0.15405 nm), with a scanning rate of 4°/min and range within 10°–80°. Scanning electron microscopy (SEM) characterization was performed on a JEOL 7500F field-emission SEM. TEM images were obtained on polymer coated copper grids by using a Tecnai 10 apparatus. Ultraviolet-visible spectrophotometer (UV-vis, Lambda-950) was employed to obtain the optical properties of the samples by UV-vis diffuse reflectance spectroscopy (DRS) in the wavelength of 300-800 nm, where $BaSO_4$ and was used as the references. Steady-state photoluminescence (PL) was performed on an Edinburgh FLS98. Time-resolved PL spectra were recorded on a Leica DMi8 system with a pulsed white light laser (SuperK Extreme EXW‑12, NKT Photonics) operating at 405 nm. Raman measurements were performed using an upright optical microscope (BX53, Olympus, Japan) equipped with a motorized stage (Märzhäuser Wetzlar GmbH, Germany) on a commercial Raman setup (MonoVista CRS+, S&I GmbH, Germany). Nitrogen adsorption-desorption isotherms were recorded using an ASAP 2420 surface area and porosity analyzer at 77 K. The specific surface area was calculated by the Brunauer-Emmett-Teller (BET) method. The pore size distribution was calculated by the Barrett-Joyner-Halenda (BJH) method. X-ray photoelectron spectroscopy (XPS) analysis was performed on a Thermo Fisher ESCALAB 250Xi instrument with a monochromatic Al Kα X-ray source (1486.6 eV).The UV-vis absorption spectra were collected by a UV-vis spectrophotometer (Perkin Elmer Lambda 35 UV-vis spectrometer). PL properties of the samples were investigated by Perkin Elmer LS45 luminescence spectrophotometer.

2.6 Photoelectrochemical Measurements

The photoelectrochemical characterizations were conducted on a three-electrode system by using computer-controlled electrochemical workstation (CHI 660E). Typically, 20 mg photocatalyst was mixed with 50 μL water and 50 μL nafion solution under ultrasonication to form a homogeneous suspension. Then, the above mixed solution (10 μL) was uniformly applied on the conductive side of ITO glass and dried

in a vacuum oven at 45°C for 1h. A three-electrode system consisting of a saturated calomel electrode (SCE), an ITO glass electrode and a Pt plate was used as the reference, working and counter electrodes, respectively. Tetrabutylammonium hexafluorophosphate (TBAPF$_6$, 0.1 M) dissolved in dichloromethane (DCM) solution was used as the electrolyte in this three-electrode system. The photocurrent-time (I-t) curves were obtained under a light on/off cycles condition. The photocurrent response versus different monochromatic light was also recorded in this three-electrode system. Generally, the light conversion into photocurrent is majorly composed of three steps including the light absorption efficiency (η_{abs}), photoinduced carrier separation rate (η_{sep}) and surface charge transfer efficiency (η_{trans}) of photocatalysts. As a result, the photocurrent intensity J_1 can be described by the following Equations [32,33]:

$$J_1 = J_{max} \times \eta_{abs} \times \eta_{sep} \times \eta_{trans} \ (1)$$

Where J_{max} represents the theoretical maximum photocurrent intensity. Because the surface charge transfer is exceedingly fast with the addition of methylviologen dichloride (MVCl$_2$) so that the η_{trans} in this case is considered as 100%, hence the photocurrent intensity in this condition can be calculated using the following equation:

$$J_2 = J_{max} \times \eta_{abs} \times \eta_{sep} \ (2)$$

As the J_{max}, η_{abs}, and η_{sep} are unchanged for the J_1 and J_2, the η_{trans} can be obtained by the following equation:

$$\eta_{trans} = J_1/J_2 \ (3)$$

2.7 Density functional theory (DFT) calculations

Density functional theory (DFT) calculations were performed by the Vienna ab initio simulation package (VASP). The exchange correlation potential was described by the Perdew-Burke-Ernzerhof(PBE)2 formulation of the generalized gradient approximation (GGA). The ion-electron interactions were represented by the projector augmented wave (PAW)3 method. The cutoff energy was set as 550 eV. The k-point sampling was performed using the Monkhorst-Pack scheme.4 The electronic self-consistent minimization was converged to 10-4 eV, and the geometry optimization was converged to -0.02 eV.

2.8 Photocatalytic activity evaluation

All the photocatalytic reactions were performed in a 25 mL quartz reactor under simulated solar light irradiation (AM 1.5G, 150 W Xe lamp). First, 10 mg catalyst and 0.1 mmol BA were added to 2.5 mL BTF solution with saturated molecular oxygen. Then, the mixture was irradiated under stirring for 4 h. Finally, the mixture was centrifuged, and the liquid was analyzed by GC setup (Shimadzu 2010). The conversion and selectivity of BA were calculated according to the equations:

$$Conversion\ (\%) = [(C_0\text{-}C_1)/C_0] \times 100\% \quad (4)$$

$$Selectivity\ (\%) = [C_2/(C_0\text{-}C_1)] \times 100\% \quad (5)$$

Where C_0 is the initial concentration of BA, and C_1 and C_2 are the concentrations of the BA and benzaldehyde (BAD) after the reaction, respectively.

3. Results and discussion

The synthesis process for the CBB-NP@P-tube-CN composite is depicted in **Fig. 1a**. As shown in **Fig S1a**, melamine powder precursor displays an aggregated structure with small irregular particles on its surface. After hydrothermal treatment, the nanorods with diameters ranging from 200-400 nm were obtained (**Fig S1b**). TEM, SEM and HAADF-STEM images (**Figs 1b-d**) suggest that the obtained material (tube-CN) presents a distinctly tubular structure with abundant pores on the wall. The diameter of hollow tube is about 150 nm. This is the first report on the C_3N_4 hollow tubes with pores in the wall. The porous structure in the wall of tube-CN originates from the release of gases (such as H_2O and CO_2) during the calcination of super-molecular nanorods [30], in which these released gases can serve as bubble template for the transformation of super-molecular nanorods into porous g-C_3N_4 nanotubes (P-tube-CN). After CBB nanoparticles loading, the tube-CN still keeps well-defined tubular configuration with CBB nanoparticles adhered on its surface (**Fig 1c**). The enlarged TEM image in **Fig 1e** demonstrates that the abundant pores are well maintained after loading CBB nanoparticles. The rich porous structure of

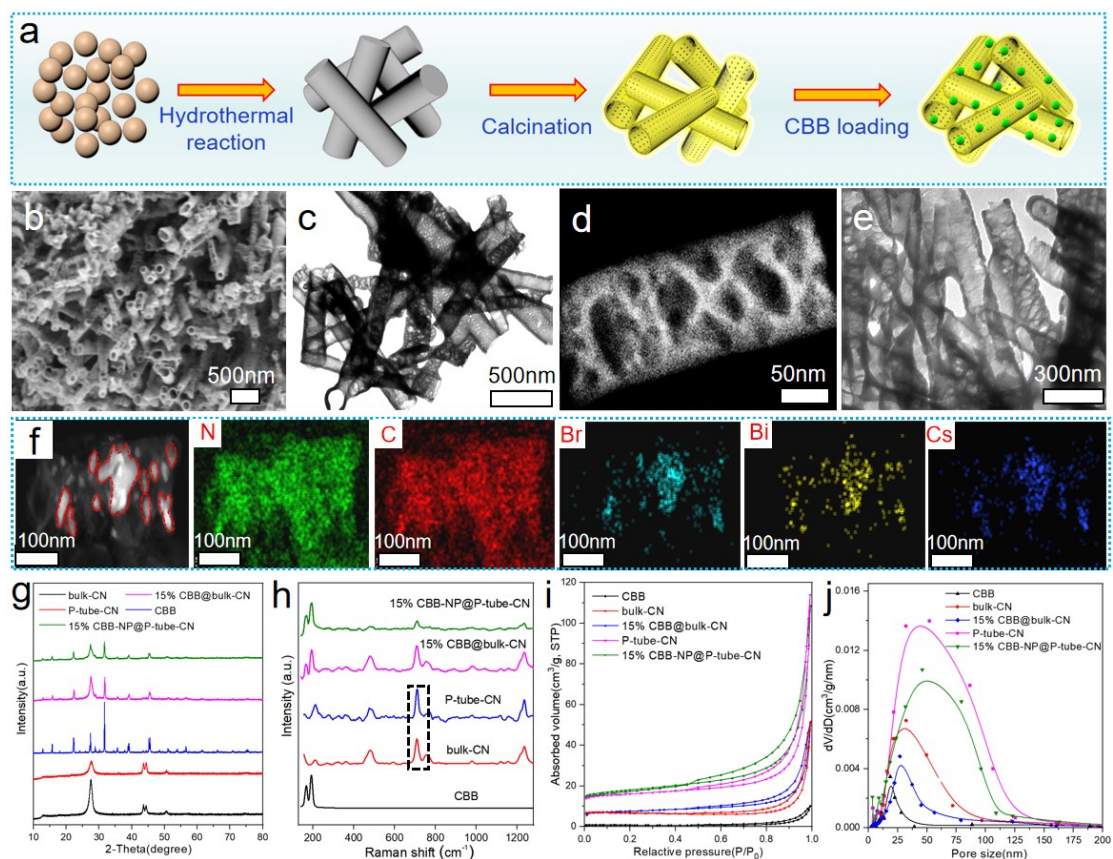CBB-NP@P-tube-CN composite is expected to endow efficient mass and charges

Fig 1. (a) Schematic diagram for the synthesis of CBB-NP@P-tube-CN composite. (b) SEM, (c) TEM and HAADF-STEM images of the tube-CN sample. (e) TEM image and (f) HAADF-STEM with corresponding elemental mapping images of the 15%CBB/tube-CN. (g) XRD patterns, (h) Raman spectra, (i) N_2 adsorption-desorption isotherms and (j) pore size distribution curves of the as-prepared samples.

transfer and enhanced interaction between light and matter, thus being profitable for efficient photocatalytic activity [37-40]. The HAADF-STEM technique is also used to reveal the micro-nanostructure of the CBB-NP@P-tube-CN composite. The tubular shape of CN tubes are well preserved after the growth of the CBB nanoparticles on the tube walls (**Figs. S2a,b,d**). As seen from the enlarged HAADF-STEM images in **Figs. S2c,e,f**, the interatomic distances of 0.7, 0.4, 0.5 and 0.9 nm corresponding to the (100), (101), (102) and (001) planes can be indexed to the phase of $Cs_3Bi_2Br_9$ compound. Furthermore, the distinct lattice fringe in **Fig. S2f** implies the good crystallinity of the loaded $Cs_3Bi_2Br_9$ nanoparticles. **Fig 1f** displays the

8

HAADF-STEM image and corresponding EDS elemental mapping pictures of the CBB-NP@P-tube-CN composite. It is clear that the bright domain (circled by red lines) is ascribed to CBB component with homogeneous distribution of Br, Bi and Cs while dark part belongs to P-tube-CN matrix with uniform distribution of C and N elements. The size of CBB-NP ranges from 20-120 nm. EDS spectrum (**Fig. S3**) shows the existence of Br, Bi, Cs, C and N elements in the CBB-NP@P-tube-CN. The above results further demonstrate the successful synthesis of tubular porous CBB-NP@P-tube-CN composite.

Fig 1g shows the XRD patterns of the as-prepared samples, two obvious diffraction peaks were found at around 13.3° and 27.7° for both bulk-CN and porous tube-CN samples, which can be ascribed to the (100) plane of the interlayer structural packing motif and the (002) plane of the interlayer stacking of conjugated aromatic units, indicating their graphite-like configuration [31-33]. Notably, porous tube-CN exhibited a weaker peak intensity and slight shift of peak to a lower degree in comparison to bulk-CN, which were attributed to the decreased crystallinity resulting from the presence of abundant porosity and the O doping in tube-CN, respectively [27,29,36]. The XRD pattern of $Cs_3Bi_2Br_9$ was in good agreement with the patterns reported in literature [10,12]. For the 15% CBB@bulk-CN and 15% CBB-NP@P-tube-CN composites, both $g-C_3N_4$ and $Cs_3Bi_2Br_9$ are present, indicating the successful hybridization between $g-C_3N_4$ and $Cs_3Bi_2Br_9$ components. The Raman spectra of the as-prepared samples are displayed in **Fig. 1h**. It can be recognized that both CBB-NP@P-tube-CN and CBB@bulk-CN composites present the characteristic peaks from CBB and C_3N_4. It is noteworthy that the peak of P-tube-CN slightly moves to a higher wavenumber compared with bulk-CN, which can be ascribed to the existence of tiny O dopant in the lattice of P-tube-CN [26,28].

The textural properties of the as-prepared samples are investigated by N_2 adsorption-desorption. As depicted in **Fig. 1i**, all the samples show the typical II adsorption isotherm with distinct adsorption-desorption hysteresis, therefore illustrating the existence of mesopores and macropores [41-43]. Compared with bulk-CN, P-tube-CN displays almost 7 times higher specific surface area of 70.5 m^2

g^{-1}, being profitable for offering more reactive sites and thus accelerating the photocatalytic process. For the 15% CBB-NP@P-tube-CN composite, its specific surface area remains the almost same in comparison to P-tube-CN due to relatively small loading concentration of CBB. As to CBB, bulk-CN and 15% CBB@bulk-CN samples, the low specific surface area can be ascribed to their intrinsically aggregated morphology. Pore size distribution curves (**Fig. 1j**) demonstrate that the tube-CN and 15% CBB-NP@P-tube-CN samples possess the much wider pore size distribution from 2 to 180 nm than that of CBB, bulk-CN and 15% CBB@bulk-CN. The results of textural properties are in good accordance with TEM observation. The more abundant pores from mesopore to macropore in 15% CBB-NP@P-tube-CN are favorable for reactant molecules transfer and diffusion, thus bringing out the improved reaction kinetics [32,33,44]. The detailed values of surface area and pore volume for the synthesized samples are listed in **Table S1**.
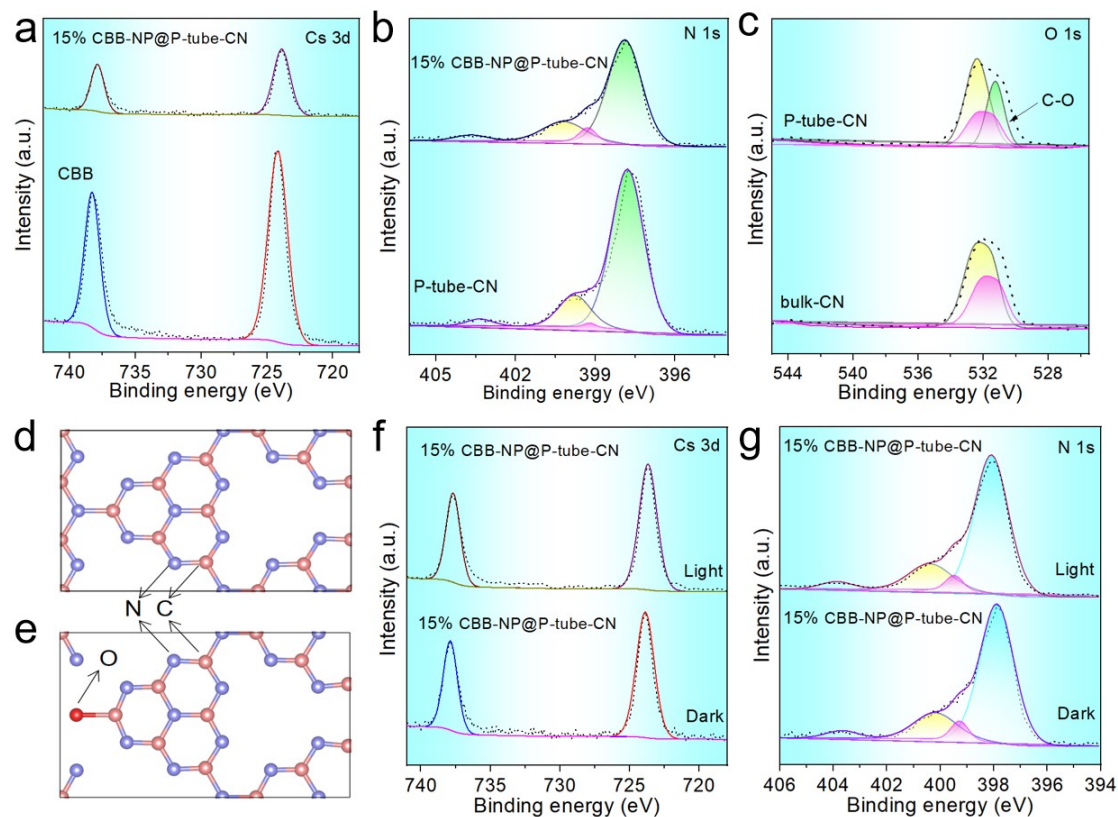

Fig 2. (a) The high-resolution XPS spectra for (a) Cs 3d, (b) N 1s and (c) O 1s. The schematic structures of (d) bulk-CN and (e) P-tube-CN. The high solution XPS spectra of (f) Cs 3d and (g) N

1s for the representative 15% CBB/tube-CN under *in-situ* light irradiation and darkness conditions.

The surface compositions and chemical states of the as-synthesized photocatalysts are characterized by XPS technique. The full XPS spectra in **Fig. S4** suggest the existence of the elements Cs, Br, Bi, C and N in CBB-NP@P-tube-CN composite, further indicating the successful fabrication of CBB-NP@P-tube-CN photocatalyst. Notably, the intensity of O 1s peak of P-tube-CN is stronger than that of bulk g-C_3N_4, illustrating more plentiful oxygen species on the surface of P-tube-CN due to its higher specific surface area and porous structure [33]. To explore the interfacial electron tendency between $Cs_3Bi_2Br_9$ and C_3N_4, high resolution XPS spectra of Cs 3d, Bi 4f, Br 3d, C 1s and N 1s in the CBB-NP@P-tube-CN hybrid and the single component are investigated and compared. As shown in **Fig. 2a** and **Figs. S5a,b**, the binding energies of Cs 3d, Bi 4f and Br 3d for CBB-NP@P-tube-CN are slightly moved to lower binding energy in comparison to pure $Cs_3Bi_2Br_9$ while the binding energies of N 1s and C 1s for CBB-NP@P-tube-CN are slightly moved to higher binding energy compared with P-tube-CN (**Fig. 2b** and **Fig. S5c**). This suggests that for the CBB-NP@P-tube-CN hybrid, Cs, Bi and Br ions of $Cs_3Bi_2Br_9$ become electron-rich and to balance the electron redistribution in the CBB-NP@P-tube-CN composite, C and N ions of tube-CN get electron-deficient. These results demonstrate the strong interfacial interactions between $Cs_3Bi_2Br_9$ and C_3N_4 due to formation of heterostructure [24,25]. The high-resolution O 1s spectrum in **Fig. 2c** displays that there are two kinds of O species in bulk g-C_3N_4. The binding energies at around 531.9 eV (for O-H) and 533.4 eV (for O-N) are ascribed to the surface hydroxyl groups and the intermediates of melamine thermal-polymerization. A new peak at lower binding energy (531.1 eV) is found in the O 1s spectrum of P-tube-CN, being attributed to the C-O and N-C-O species in lattice [29]. This result indicates that O replaces N and links with C in the basic aromatic units of P-tube-CN. The origin of O dopant in P-tube-CN can be ascribed to the adhered water molecule on super-molecular nanorods. The post calcination of super-molecular nanorods leads to the production of O doping in the lattice of C_3N_4. The basic units of bulk-CN and P-tube-CN can be

proposed (**Figs. 2d,e**) according to XPS results, which were used as the models for the subsequent theoretical calculations. In order to reveal the photoinduced charges migration direction between $Cs_3Bi_2Br_9$ nanoparticles and P-tube-CN, the *in-situ* irradiated XPS analysis under light irradiation is carried out. As depicted in **Fig. 2f**, the binding energy of Cs 3d in CBB-NP@P-tube-CN shows a negative shift under light irradiation compared with that in dark conditions, indicating the electron accumulation around the nuclei of Cs. Meanwhile, the external light illumination leads to a positive shift of binding energy for N 1s (**Fig. 2g**), suggesting that the photoinduced electron migration from P-tube-CN to CBB nanoparticles via the CBB-NP@P-tube-CN interface [28].
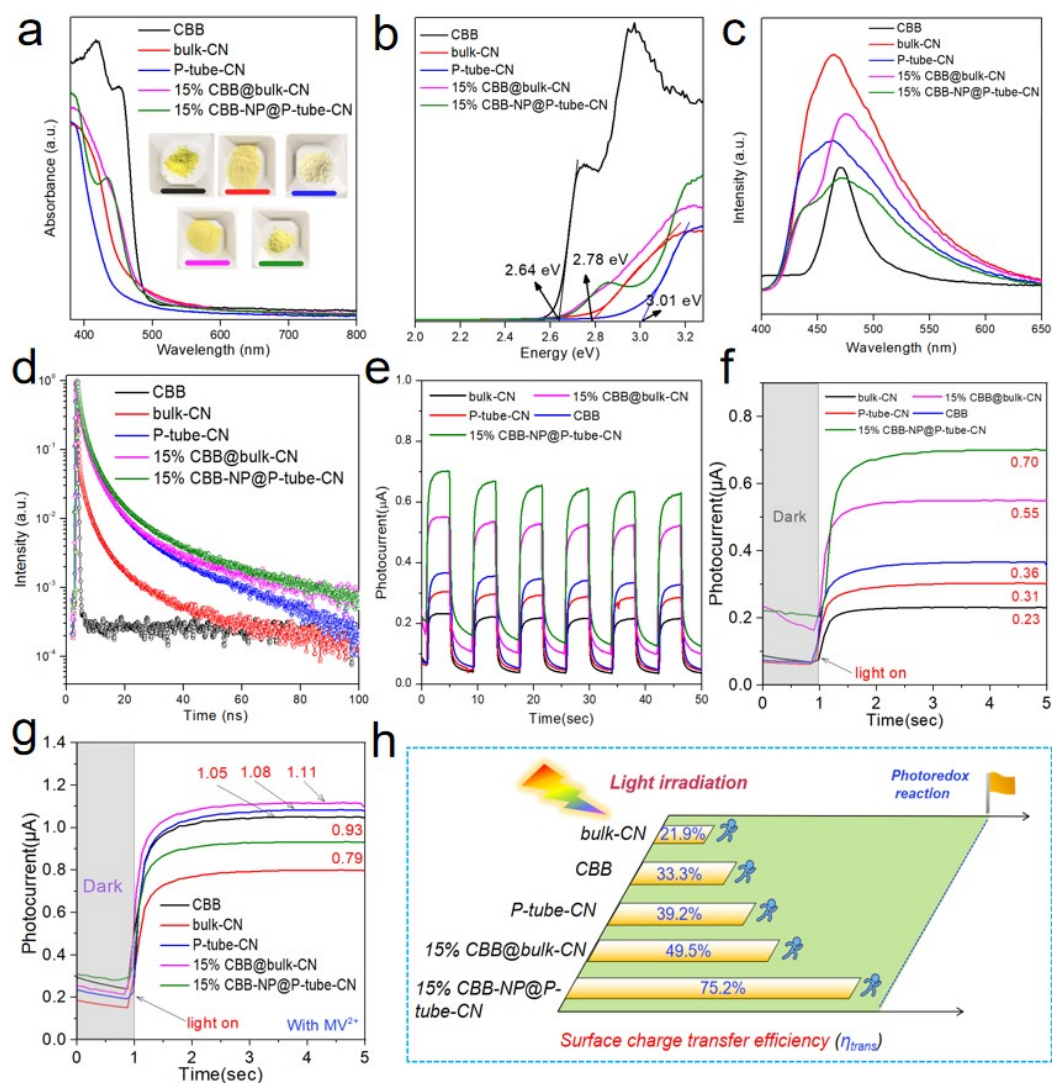

Fig 3. UV-Vis absorption spectra (Insets are the photographs of the prepared samples), Tauc plots curves, PL spectra and PL decay spectra of the synthesized samples. (e) Photocurrent response

1

curves, (f) photocurrent density of the obtained samples under visible light irradiation (f) without and (g) with $MVCl_2$. (h) The calculated η_{trans} of the prepared photocatalysts.

The optical properties and band gap structures of the as-prepared photocatalysts have been studied (**Fig. 3a,b**). As shown in **Fig. 3a**, the absorption edges of pristine $Cs_3Bi_2Br_9$ and C_3N_4 tube locate at around 520 and 440 nm, respectively, suggesting the much broader visible light response of $Cs_3Bi_2Br_9$ than that of C_3N_4 tube. A blue shift of absorption band of C_3N_4 tube in comparison to that of bulk C_3N_4 is ascribed to the fact that O dopant in C_3N_4 tube leads to the broadened band gap and more negative VB position, being favorable for offering enough photoredox driven force and thus accelerating the photocatalytic reaction. With $Cs_3Bi_2Br_9$ loading, the obtained $Cs_3Bi_2Br_9@C_3N_4$ composites show the red-shift of absorption edge compared with that of single C_3N_4, indicating that the heterostructure engineering has a great influence on the electronic structure of photocatalyst. Meanwhile, the deeper colors of the hybrid samples in comparison to single C_3N_4 further indicate the enhanced visible light absorption ability [40]. The band gap values of these samples are calculated from the transformed Kubelka-Munk formula [38] as listed in **Table S1**. The photoluminescence (PL) and PL decay spectra are detected to disclose the separation of the photoinduced carriers [8-10]. As shown in **Fig. 3c**, g-C_3N_4 and Cs_3BiBr_9 show the characteristic PL emission peaks at around 455 nm and 470 nm, respectively. The weaker PL intensity of C_3N_4 tube compared with bulk g-C_3N_4 is attributed to the generated new energy level stemming from O doping and the unique tubular architecture inducing fast photoinduced charges separation [29]. Among all the prepared samples, 15% CBB-NP@P-tube-CN displays the lowest PL intensity, indicating that the synergy between oxygen doping, porous tubular structure and heterostructure engineering results in fast photogenerated carrier separation. Moreover, the formed heterostructure in $Cs_3Bi_2Br_9@C_3N_4$ composites has a great influence on the electronic structure of photocatalyst, thus delivering different PL profile between CBB-NP@P-tube-CN and P-tube-CN samples. PL decay spectra are also recorded to reveal the charge dynamic behavior on the synthesized samples (**Fig. 3d**). As listed in **Table S1**, the average PL lifetimes of the prepared samples are as follows: 15%

CBB-NP@P-tube-CN>15% CBB@bulk-CN>P-tube-CN>bulk-CN>CBB. The PL decay spectrum results suggest the fastest carrier separation and transport ability of the CBB-NP@P-tube-CN photocatalyst, which is associated with the merits of heterostructure engineering, porous structure and oxygen doping [39,40]. To further reveal the photoexcited carrier separation ability for the synthesized samples, the photocurrent characterization is conducted (**Fig. 3e**). It is observed that the photocurrent signals of all photocatalysts are coincident and repeatable, implying their reliable photoelectric response ability. The order of photocurrent densities of these photocatalysts is arranged in the following order: bulk-CN < P-tube-CN < CBB < 15% CBB@bulk-CN < 15% CBB-NP@P-tube-CN. Compared with bulk C_3N_4, porous C_3N_4 nanotubes with unique structure present faster photoinduced carriers separation and migration ability, therefore enabling higher photocurrent intensity. The highest photocurrent response of 15% CBB-NP@P-tube-CN illustrates its efficient carrier separation and minimum carrier recombination performance, which is in good agreement with the PL and PL lifetime characterization results. Commonly, the photocatalytic activity depends on the synergistic effect of light absorption (η_{abs}), carrier separation (η_{sep}) and surface charge transfer rate (η_{trans}). For a photocatalyst, η_{trans} is deemed as the most crucial factor [12,13,27]. Herein, we investigate the η_{trans} value of the obtained photocatalysts via an elaborately designed photocurrent test system (See Experimental section) with $MVCl_2$ as a rapid electron scavenger [32]. As depicted in **Fig. 3f**, the 15% CBB-NP@P-tube-CN shows a photocurrent density of 0.70 μA, being 1.3, 1.9, 2.3 and 3.0 times higher than that of 15%CBB@bulk-CN (0.55 μA), CBB (0.36 μA), P-tube-CN (0.31 μA) and bulk-CN (0.23 μA), respectively. **Fig. 3g** presents that the photocurrent density increases to 0.93 μA with the addition of $MVCl_2$ (methylviologen dichloride) for 15% CBB-NP@P-tube-CN. Meanwhile, other photocatalysts also show various degrees of improvement in photocurrent density. Notably, 15% CBB@bulk-CN, CBB and bulk-CN display even higher photocurrent intensities than that of 15% CBB/tube-CN with the addition of $MVCl_2$, being ascribed to that their largely limited η_{trans} is fully released, indicating also that the values of η_{trans} for the three photocatalysts are much lower than that of 15%

1

CBB-NP@P-tube-CN in the normal conditions. From the Equations (1-3) in Experimental section, the η_{trans} of 15%CBB/tube-CN is thus calculated to be 75% (**Fig. 3h**), being around 1.5, 2.3, 1.9 and 3.4 folds higher than that of 15% CBB@bulk-CN (49.5%), CBB (33.3%), P-tube-CN (39.2%) and bulk-CN (21.9%), respectively. As a result, the 15% CBB-NP@P-tube-CN possesses a superior injection efficiency of photogenerated charge carriers into the photocatalytic system and an outstanding photocurrent density. All the above results demonstrate that CBB and CN hybridization can drastically enhance the visible light harvesting, facilitate photoexcited carrier dissociation and charge migration as well as the injection rate of the photoexcited charge carriers, and that 15% CBB-NP@P-tube-CN photocatalyst shows the best characteristics.
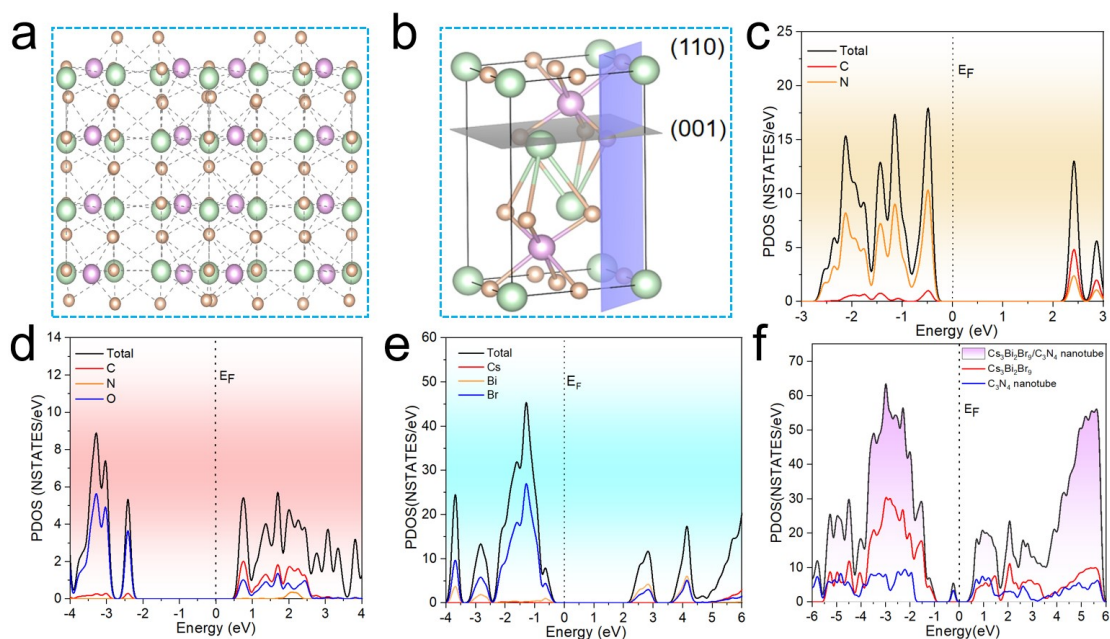

Fig 4. (a) Schematic unit cell of the $Cs_3Bi_2Br_9$ and (b) constructed model for the theoretical calculations (Green, brown and purple balls represent Cs, Br and Bi atoms, respectively). The density of states (DOS) of (d) P-tube-CN, (e) $Cs_3Bi_2Br_9$ and (f) $Cs_3Bi_2Br_9@C_3N_4$ nanotube.

DFT calculation was carried out to study the influence of heterostructure construction on the electronic band gap structure and photoinduced electron migration of the hybrid photocatalyst [30,32]. The schematic unit cell of $Cs_3Bi_2Br_9$ and constructed model calculation are adopted for theoretical calculations (**Figs. 4a, b**). As shown in **Fig. 4c**, the band gap of bulk-CN is calculated from the theoretical

simulation to be about 2.6 eV. The poor overlap between the C and N atoms in bulk-CN sample would bring out the poor carrier density and photoresponse capability, therefore being disadvantageous for photocatalytic ability, which are in accordance with previous reports and experimental results [26,27]. Compared with bulk-CN, the slight increase of band gap (about 2.7 eV) for tube-CN acquired from DOS simulation is observed (**Fig. 4d**), which is consistent with UV-vis absorption results and ascribed to the role of O doping. In addition, the conduction band (CB) of P-tube-CN is recognized to be composed of overlap between the C and N orbitals, while the valence band (VB) predominantly consists of a characteristic of O orbital with negligible overlap with the C and N atoms (**Fig. 4d**), suggesting that the O dopant exerts a major function on the formation of CB and VB of C_3N_4. The DOS simulation of $Cs_3Bi_2Br_9$ is shown in **Fig. 4e**. The calculated band gap value is around 2.5 eV, which is consistent with previous publications and experimental results [12]. For CBB-NP@P-tube-CN hybrid, a midgap state stemming from O doping near the Fermi level (E_F) can be observed (**Fig. 4f**), being favorable for the convenient photoinduced electron transfer from VB to CB and the prohibited electron-hole pair recombination. Moreover, the incorporation of CBB into P-tube-CN leads to a significant improvement in DOS at both VB and CB, giving rise to the enhanced charge carrier concentration and good photoresponse ability for increased photocatalytic performance, being in excellent agreement with the above photoelectrochemical characterizations.

Photocatalytic benzyl alcohol (BA) oxidation is carried out under full solar spectrum illumination using an AM 1.5G lighter. Benzaldehyde is detected as the major product over all the prepared photocatalysts with almost 100% selectivity as depicted in **Fig. 5a**. The BA conversion over the CBB, bulk-CN and P-tube-CN samples is quite low. The 15% CBB-NP@P-tube-CN hybrid shows the best photocatalytic activity, being about 14, 19 and 2.8 times higher photocatalytic BA conversion than that of CBB, P-tube-CN and 15% CBB@bulk-CN nanotubes photocatalysts, respectively. As to the 15% CBB@bulk-CN composite, its higher BA conversion efficiency compared with those of P-tube-CN and bulk-CN can be

ascribed to the formation of heterostructure for fast photoinduced carriers separation. The amount of CBB loading is also studied. With increasing the CBB loading, the CBB-NP@P-tube-CN hybrids show the gradually increased BA conversion with the optimal CBB loading percent of 15% (**Fig. S6**). The photocatalytic BA conversion performance is attenuated when the CBB loading percent is over 15%, which may be attributed to that the excessive CBB results in the shielding of the surface active sites for P-tube-CN [45-47]. The CBB-NP@P-tube-CN photocatalyst used for the photocatalytic reaction for 10 consecutive cycles of 40 h showed great chemical and physical stability (**Fig. S7a**). Moreover, the hybrid photocatalyst also displays excellent activity after storage for 30 days (**Fig. S7b**).
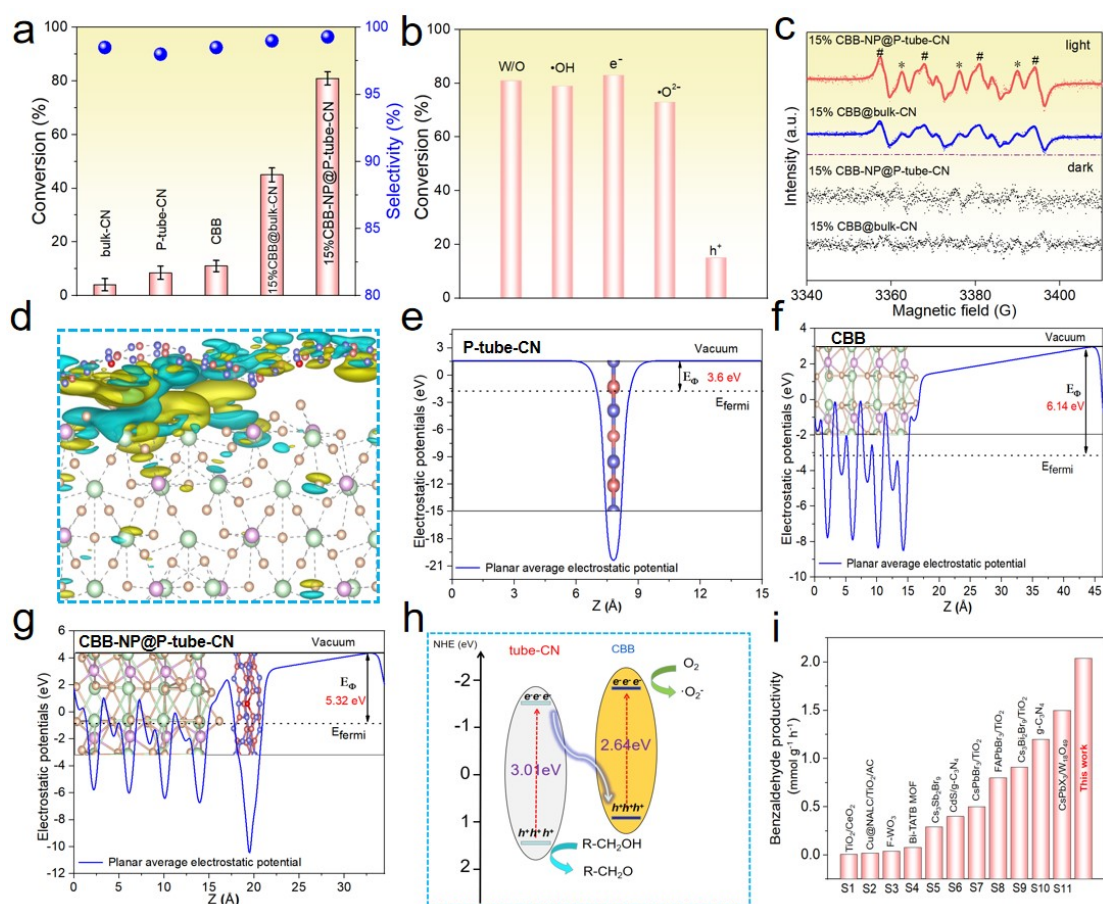

Fig 5. (a) Photocatalytic benzyl alcohol conversion and the corresponding selectivity over the as-prepared photocatalysts. (b) photocatalytic benzyl alcohol conversion with the addition of various scavengers over the optimal 15% CBB-NP@P-tube-CN. (c) DMPO-captured superoxide radical (#) and nitroxide like radical (*) EPR spectra of 15% CBB@bulk-CN and 15% CBB-NP@P-tube-CN. (d) Electron density difference image of the $Cs_3Bi_2Br_9$/tube-CN interface

(The yellow and cyan regions denote electron accumulation and depletion, respectively. The green, brown and purple balls represent Cs, Br and Bi atoms, respectively). Electrostatic potential energy plots for (e) P-tube-CN, (f) CBB, and (g) CBB-NP@P-tube-CN heterojunction. (h) Schematic process for photocatalytic benzyl alcohol conversion into benzaldehyde over the CBB-NP@P-tube-CN photocatalysts. (i) The comparison of benzaldehyde productivity via photocatalytic alcohol oxidation over the CBB-NP@P-tube-CN nanotubes and other photocatalysts.

To reveal the involved active species during the photocatalytic BA conversion, photocatalytic BA oxidation over the 15% CBB-NP@P-tube-CN with the addition of various scavengers is conducted. As shown in **Fig. 5b**, the benzyl alcohol oxidation activity slightly changes with the presence of hydroxyl, electron and superoxide radical scavengers. However, with the introduction of the hole scavenger, the BA oxidation ability is significantly reduced, suggesting that the photoinduced holes play a crucial function in benzyl alcohol oxidation reaction. The produced active oxygen related radicals during the photocatalytic reaction was revealed by electron spin resonance (ESR) spectroscopy with 5,5-dimethyl-1-pyrroline N-oxide (DMPO) as the trapping agent. As shown in **Fig. 5c**, the ESR signals of $^{\bullet}O^{2-}$ species in 15% CBB-NP@P-tube-CN were detected under visible light illumination, being attributed to O_2 reduction by the photoinduced electrons. In addition to $^{\bullet}O^{2-}$ species, the signals for nitroxide radicals were also found due to light-excited tailoring of the N-C bond and the disassociation of DMPO-$^{\bullet}O^{2-}$ adduct [5]. No oxygen related radicals were found under dark conditions. The similar result was found in 15% CBB@bulk-CN. When the test was conducted under visible light, the $^{\bullet}O_2^{-}$ species were also detected due to the O_2 reduction. Notably, the stronger signals for nitroxide radicals of 15% CBB-NP@P-tube-CN than 15% CBB@bulk-CN were recognized owing to higher photoexcited electron concentration on the CB of CBB, further indicating the efficient carrier separation on CBB-NP@P-tube-CN and being favorable for subsequent photoredox reaction [33]. In addition to BA conversion, the optimal 15% CBB-NP@P-tube-CN also exhibits very good capability for photocatalytic conversion of other benzylic alcohols into corresponding aldehyde with excellent selectivity (**Fig.**

S8), demonstrating its versatile characteristics in photosynthesis of value-added organics.

The electron density difference simulation on the interface between CBB and P-tube-CN was conducted to reveal the electron distribution and migration in the heterostructure (**Fig 5d**). It is clearly observed that the electrons are inclined to shift from P-tube-CN to CBB. To obtain more details about the generated heterojunction between the P-tube-CN and CBB, electrostatic surface potential energy plots were studied. It is found that P-tube-CN presents a work function value (Φ) of 3.6 eV (**Fig. 5e**) vs. vacuum level, while CBB displays a higher work function of 6.14 eV (**Fig. 5f**). The difference values in work function can result in electron move from the P-tube-CN to $Cs_3Bi_2Br_9$, leading to a band bending and generating a redistributed charge region [27,38]. The work function of CBB-NP@P-tube-CN is calculated to be 5.32 eV (**Fig. 5g**) because of the equilibrum of Fermi levels and charge shift at the heterojunction interface, further demonstrating the strong delocalization of electrons owing to the generation of heterostructure. To investigate the photocatalytic mechanism, the band gap configuration and detailed energy level position of the CBB-NP@P-tube-CN hybrid were studied. The VB positions of the as-prepared samples were studied via the XPS valence band spectrum. As shown in **Fig. S9**, the VB levels of the as-prepared bulk-CN, P-tube-CN and CBB are determined to be 1.23, 1.49 and 0.95 eV, respectively. Of note, the P-tube-CN presents a more positive VB level than that of bulk-CN, thus endowing much stronger photo-oxidation ability [48-52]. The band gaps of P-tube-CN and CBB, calculated from the corresponding Tauc plots (**Fig. 3b**), are 3.01, and 2.64 eV, respectively. According to the band gap and VB position, the band gap configuration of the CBB-NP@P-tube-CN hybrid is presented in **Fig. 5h**. Based on the above analyses, the mechanism of photogenerated electron-hole pairs separation and transfer on CBB-NP@P-tube-CN via a Z-scheme pathway is proposed. Under visible light illumination, both CBB and P-tube-CN can produce the photoexcited electrons on their CB with holes on their VB. According to the *in-situ* XPS results, the formed photoelectrons on the CB of P-tube-CN are shifted to the VB of CBB due to the different work function between the two components,

remaining the photoelectrons on the CB of CBB and the holes on the VB of P-tube-CN, respectively. This typical Z-scheme heterojunction significantly improves both the oxidative and the reductive potentials. Owing to the fast carrier separation, $\cdot O_2^-$ is more efficiently produced on the CB of CBB. Meanwhile, the holes on the VB of P-tube-CN participate in the BA oxidation into benzaldehyde evolution. Notably, the CBB-NP@P-tube-CN endows much stronger photo-oxidation ability than that of CBB@bulk-CN because the O dopant in P-tube-CN component leads to more positive VB level, thus being favorable for the efficient and direct one-step oxidation benzylic alcohol into benzaldehyde [6,7,13]. As illustrated in **Fig. S10**, combining the synergistic effects of enhanced light harvesting from Cs_3BiBr_9 loading, increased interaction between light and matter, facile mass diffusion and electrons transfer from the porous tubular structure as well as enhanced photo-oxidation ability, the CBB-NP@P-tube-CN photocatalysts show their exceptional photocatalytic performance for benzyl alcohol selective oxidation. Finally, the comparison of benzaldehyde productivity via photocatalytic alcohol oxidation over our CBB-NP@P-tube-CN and other photocatalysts is shown in **Fig. 5i** and **Table S2**. It is clear that our CBB-NP@P-tube-CN gives the best photocatalytic benzaldehyde productivity compared to other perovskite and C_3N_4 based photocatalysts reported in the literature, indicating its great potential for practical industrial photocatalytic benzaldehyde preparation.

Conclusions

In summary, Z-Scheme CBB-NP@P-tube-CN heterojunction photocatalyst demonstrates the exceptional photocatalytic performance for benzylic alcohols oxidation into benzaldehyde with high selectivity (over 99%). The favorable porous tubular configuration could offer the high mass and ions diffusion kinetics, and the Z-Scheme heterojunction on the interface between CBB and P-tube-CN provides the efficient photoinduced carriers dissociation and sufficient photoredox potentials. As a result, the optimized 15% CBB-NP@P-tube-CN hybrid gives rise to the highest photocatalytic BA conversion rate, being about 14, 19 and 3 times higher photocatalytic benzylic alcohols conversion than that of CBB, P-tube-CN and

CBB@bulk C_3N_4 nanotubes photocatalysts, respectively. The CBB-NP@P-tube-CN photocatalyst also presents excellent cycling stability. In the photocatalytic selective oxidation of other aromatic alcohols, such photocatalysts also show excellent activity and selectivity. This work proposes an effective strategy to fabricate photocatalyst with accelerated separation of photoinduced carriers and promoted photoredox ability for the efficient photocatalytic value-added organics synthesis.

CRediT authorship contribution statement

Y.D. and C.W. contributed equally to this work. Y.D. designed the experiments, wrote the original draft of the manuscript, and did the data analysis. C.W., S.B., L.P., R.Z., and Y.H.N. carried out the synthesis of the materials, PL testing, review of the writing, and investigation of DFT calculations. D.A.E., S.B., and G.V.T. investigated TEM characterization and reviewed the writing. J.Z., J.H., and M.R. reviewed and edited the writing. L.H.C and B.L.S. supervised the project and also reviewed and edited the writing. All authors discussed and commented on the final version of the manuscript.

Conflicts of interest

There are no conflicts to declare.

Reference

1. U. Sanyal, S. F. Yuk, K. Koh, M. S. Lee, K. Stoerzinger, D. Zhang, J. A. Lercher, Hydrogen bonding enhances the electrochemical hydrogenation of benzaldehyde in the aqueous phase, Angew. Chem. Int. Ed. 133 (2021) 294-300.

2. G. Cheng, A. Jentys, O. Y. Gutiérrez, Y. Liu, Y. H. Chin, J. A. Lercher, Critical role of solvent-modulated hydrogen-binding strength in the catalytic hydrogenation of benzaldehyde on palladium, Nature Catal. 4 (2021) 976-985.

3. R. Connon, B. Roche, B. V. Rokade, P. J. Guiry, Further developments and applications of oxazoline-containing ligands in asymmetric catalysis, Chem Rev. 121 (2021) 6373-6521.

4. G. Berionni, Future prospects in boron chemistry: new boron compounds and Lewis acids for catalysis and materials science, Chem Syn. 1 (2021) 1-6.

5. M. H. Sun, J. Zhou, Z. Y. Hu, L. H. Chen, L. Y. Li, Y. D. Wang, B-L. Su, Hierarchical zeolite single-crystal reactor for excellent catalytic efficiency, Matter 3 (2020) 1226-1245.

6. J. A. Steele, T. Braeckevelt, V. Prakasam, G. Degutis, H. Yuan, H. Jin, M. B. Roeffaers, An embedded interfacial network stabilizes inorganic $CsPbI_3$ perovskite thin films, Nature Commun. 13 (2022) 7513.

7. B. Ghosh, D. Tay, M. B. Roeffaers, N. Mathews, Lead-free metal halide (halogenidometallate) semiconductors for optoelectronic applications, Appl. Phys. Rev. 10 (2023) 031312.

8. Q. Yang, T. Wang, Z. Zheng, B. Xing, C. Li, B. Li, Constructing interfacial active sites in $Ru/g-C_3N_{4-x}$ photocatalyst for boosting H_2 evolution coupled with selective benzyl-alcohol oxidation, Appl. Catal. B 315 (2022) 121575.

9. N. Han, X. Zhang, C. Zhang, S. Feng, W. Zhang, W. Guo, B-L. Su, Lowering the kinetic barrier via enhancing electrophilicity of surface oxygen to boost acidic oxygen evolution reaction, Matter 7 (2024) 1330-1343.

10. C. Wang, Y. Ding, B. Liu, B. Weng, J. Hofkens, M. B. Roeffaers, Crystal structure engineering of metal halide perovskites for photocatalytic organic synthesis, Chem. Commun. 59 (2023) 3122-3125.

11. M. Gebruers, C. Wang, R. A. Saha, Y. Xie, I. Aslam, L. Sun, M. B. Roeffaers, Crystal phase engineering of Ru for simultaneous selective photocatalytic oxidations and H_2 production, Nanoscale 15 (2023) 2417-2424.

12. C. Wang, B. Weng, Y. Liao, B. Liu, M. Keshavarz, Y. Ding, M. B. Roeffaers, Simultaneous photocatalytic H_2 generation and organic synthesis over crystalline-amorphous Pd nanocube decorated $Cs_3Bi_2Br_9$, Chem. Commun. 58 (2022) 10691-10694.

13. C. Wang, B. Weng, M. Keshavarz, M. Q. Yang, H. Huang, Y. Ding, M. B. Roeffaers, Photothermal Suzuki coupling over a metal halide perovskite/Pd nanocube composite catalyst, ACS Appl. Mater. Interfaces 14 (2022) 17185-17194.

14. X. Chen, Z. Sun, B. Cai, X. Li, S. Zhang, D. Fu, H. Zeng, Substantial Improvement of Operating Stability by Strengthening Metal-Halogen Bonds in Halide Perovskites, Adv. Funct. Mater. 32 (2022) 2112129.

15. Y. Ding, Y. Ye, C. Wang, L. Pei, Q. Mao, M. Liu, R. Zheng, A. Bokhari, N. Han, J. Zhong, "Light battery" role of long afterglow phosphor for round-the-clock environmental photocatalysis, J. Cleaner Prod. 450 (2024) 142041.

16. Z. Han, W. Fu, Y. Zou, Y. Gu, J. Liu, B. Huang, H. Zeng, Oriented perovskite growth regulation enables sensitive broadband detection and imaging of polarized photons covering 300-1050 nm, Adv. Mater. 33 (2021) 2003852.

17. Y. Ding, X. Lu, S. Maitra, Y. Wang, L. Pei, Q. Mao, M. Liu, J. Zhong, D. Chen, Suppressing Self-Oxidation of Eu^{2+} in Li_2CaSiO_4 for Full-Spectrum Lighting and Accurate Temperature Sensing, Laser & Photonics Rev. 18 (2024) 2400296.

18. D. Feng, X. Li, L. Zhang, Z-A. Qiao, Self-assembly method for two-dimensional mesoporous materials: a review for recent progress, Chem. Synth. 3 (2023) 2-16.

19. L. Pei, Z. Luo, X. Wang, Z. Ma, Y. Nie, J. Zhong, D. Yang, S. Bandaru, B-L Su, Tunable CO_2-to-syngas conversion via strong electronic coupling in S-scheme $ZnGa_2O_4/g-C_3N_4$ photocatalysts, J. Colloid Interface Sci. 652 (2023) 636-645.

20. D. Zhang, Q. Zhang, Y. Zhu, S. Poddar, Y. Zhang, L. Gu, Z. Fan, Metal halide perovskite nanowires: Synthesis, integration, properties, and applications in optoelectronics, Adv. Energy Mater. 13 (2022) 2201735.

21. L. Romani, A. Speltini, C. N. Dibenedetto, A. Listorti, F. Ambrosio, E. Mosconi, L Malavasi, Experimental Strategy and Mechanistic View to Boost the Photocatalytic Activity of $Cs_3Bi_2Br_9$ Lead-Free Perovskite Derivative by g-C_3N_4 Composite Engineering, Adv. Funct. Mater. 31 (2021) 2104428.

22. Y. Wang, H. Huang, Z. Zhang, C. Wang, Y. Yang, Q. Li, D. Xu, Lead-free perovskite $Cs_2AgBiBr_6$@ g-C_3N_4 Z-scheme system for improving CH_4 production in photocatalytic CO_2 reduction, Appl. Catal. B 282 (2021) 119570.

23. J. Wang, J. Wang, N. Li, X. Du, J. Ma, C. He, Z. Li, Direct Z-scheme 0D/2D heterojunction of $CsPbBr_3$ quantum dots/Bi_2WO_6 nanosheets for efficient photocatalytic CO_2 reduction, ACS Appl. Mater. Interfaces 12 (2020) 31477-31485.

24. Y. F. Mu, C. Zhang, M. R. Zhang, W. Zhang, M. Zhang, T. B. Lu, Direct Z-scheme heterojunction of ligand-free $FAPbBr_3$/α-Fe_2O_3 for boosting photocatalysis of CO_2 reduction coupled with water oxidation, ACS Appl. Mater. Interfaces 13 (2021) 22314-22322.

25. J. T. DuBose, P. V. Kamat, Efficacy of Perovskite Photocatalysis: Challenges to Overcome, ACS Energy Lett. 7 (2022) 1994-2011.

26. Y. Ding, C. Wang, L. Pei, S. Maitra, Q. Mao, R. Zheng, B-L. Su, Emerging heterostructured C_3N_4 photocatalysts for photocatalytic environmental pollutant elimination and sterilization, Inorg. Chem. Front. 10 (2023) 3756-3780.

27. C. Feng, L. Tang, Y. Deng, J. Wang, J. Luo, Y. Liu, J. Wang, Synthesis of leaf-vein-like g-C_3N_4 with tunable band structures and charge transfer properties for selective photocatalytic H_2O_2 evolution, Adv. Funct. Mater. 30 (2020) 2001922.

28. Y. Ding, S. Maitra, S. Halder, C. Wang, R. Zheng, T. Barakat, B-L. Su, Emerging semiconductors and metal-organic-compounds-related photocatalysts for sustainable hydrogen peroxide production, Matter 5 (2022) 2119-2167.

29. Y. Xiao, G. Tian, W. Li, Y. Xie, B. Jiang, C. Tian, H. Fu, Molecule self-assembly synthesis of porous few-layer carbon nitride for highly efficient photoredox catalysis, J. Am. Chem. Soc. 141 (2019) 2508-2515.

30. Y. Ding, S. Maitra, D. A. Esteban, S. Bals, H. Vrielinck, T. Barakat, B-L. Su, Photochemical production of hydrogen peroxide by digging pro-superoxide radical

carbon vacancies in porous carbon nitride, Cell Rep. Phys. Sci. 3 (2022) 100874.

31. F. Lin, S. Zhou, G. Wang, J. Wang, T. Gao, Y. Su, C. P. Wong, Electrostatic self-assembly combined with microwave hydrothermal strategy: construction of 1D/1D carbon nanofibers/crystalline g-C_3N_4 heterojunction for boosting photocatalytic hydrogen production, Nano Energy 99 (2022) 107432.

32. Y. Ding, S. Maitra, C. Wang, R. Zheng, M. Zhang, T. Barakat, B-L. Su, Hydrophilic bi-functional B-doped g-C_3N_4 hierarchical architecture for excellent photocatalytic H_2O_2 production and photoelectrochemical water splitting, J Energy Chem. 70 (2022) 236-247.

33. Y. Yin, X. Kang, B. Han, Two-dimensional materials: synthesis and applications in the electro-reduction of carbon dioxide, Chem. Synth. 2 (2022) 2-26.

34. Y. Ding, C. Wang, R. Zheng, S. Maitra, G. Zhang, T. Barakat, L. H. Chen, Three-dimensionally ordered macroporous materials for photo/electrocatalytic sustainable energy conversion, solar cell and energy storage, EnergyChem 4 (2022) 100081.

35. D. Adekoya, M. Li, M. Hankel, C. Lai, M. S. Balogun, Y. Tong, S. Zhang, Design of a 1D/2D C_3N_4/rGO composite as an anode material for stable and effective potassium storage, Energy Storage Mater. 25 (2020) 495-501.

36. Y. Ding, S. Maitra, C. Wang, S. Halder, R. Zheng, T. Barakat, B-L. Su, Vacancy defect engineering in semiconductors for solar light-driven environmental remediation and sustainable energy production, Interdiscip. Mater. 1 (2022) 213-255.

37. M. H. Sun, S. S. Gao, Z. Y. Hu, T. Barakat, Z. Liu, S. Yu, B-L. Su, Boosting molecular diffusion following the generalized Murray's Law by constructing hierarchical zeolites for maximized catalytic activity, Nat. Sci. Rev. 9 (2022) nwac236.

38. Y. Ding, S. Maitra, C. Wang, R. Zheng, T. Barakat, S. Roy, B-L. Su, Bi-functional Cu-TiO_2/CuO photocatalyst for large-scale synergistic treatment of waste sewage containing organics and heavy metal ions, Sci. China Mater. 66 (2023) 179-192.

39. S. Qu, H. Wu, Y. H. Ng, Clean Production of Hydrogen Peroxide: A Heterogeneous Solar-Driven Redox Process, Adv. Energy Mater. (2023) 2301047,

1-40.

40. Y. Ding, L. Huang, T. Barakat, B-L. Su, A novel 3DOM TiO_2 based multifunctional photocatalytic and catalytic platform for energy regeneration and pollutants degradation, Adv. Mater. Interfaces 8 (2021) 2001879.

41. W. P. Utomo, M. K. Leung, Z. Yin, H. Wu, Y. H. Ng, Advancement of Bismuth-Based Materials for Electrocatalytic and Photo (electro) catalytic Ammonia Synthesis, Adv. Funct. Mater. 32 (2022) 2106713.

42. H. Wu, X. Y. Kong, X. Wen, S. P. Chai, E. C. Lovell, J. Tang, Y. H. Ng, Metal-Organic Framework Decorated Cuprous Oxide Nanowires for Long-lived Charges Applied in Selective Photocatalytic CO_2 Reduction to CH_4, Angew. Chem. Int. Ed. 133 (2021) 8536-8540.

43. Q. C. Wei, Y. Chen, Z. Wang, D. Z. Yu, W. H.Wang, J. Q. Li, B-L. Su, Light-Assisted Semi-Hydrogenation of 1, 3-Butadiene with Water, Angew. Chem. Int. Ed. 134 (2022) e202210573.

44. H. Zhao, J. Liu, N. Zhong, S. Larter, Y. Li, M. G. Kibria, J. Hu, Biomass Photoreforming for Hydrogen and Value-Added Chemicals Co-Production on Hierarchically Porous Photocatalysts, Adv. Energy Mater. 13 (2023) 2300257.

45. D. Grammatico, A. J. Bagnall, L. Riccardi, M. Fontecave, B-L. Su, L. Billon, Heterogenised molecular catalysts for sustainable electrochemical CO_2 reduction, Angew. Chem. Int. Ed. 61 (2022) e202206399.

46. Y. Ding, L. Liang, N. Han, C. Wang, M. Liu, S. Maitra, J. Zhong, The "photons storage pool" effect of long afterglow phosphor for round-the-clock photocatalytic clean energy evolution, J. Environ. Chem. Eng. 12 (2024) 113111.

47. Y. Q. Yan, Y. Chen, Z. Wang, L. H. Chen, H. L. Tang, B-L. Su, Electrochemistry-assisted selective butadiene hydrogenation with water, Nature Commun. 14 (2023) 2106.

48. Y. Ding, C. H. Wang, J. S. Zhong, Q. N. Mao, R. T. Zheng, Y. H. Ng, B-L. Su, Three-dimensionally ordered macroporous materials for pollutants abatement, environmental sensing and bacterial inactivation, Sci. China Chem. 66 (2023) 1-19.

49. X. Yu, Z. Yu, H. Zhao, I. Gates, J. Hu, Photothermal catalytic H_2 production over

hierarchical porous $CaTiO_3$ with plasmonic gold nanoparticles, Chem. Synth. 3 (2023) 2-11.

50. C. Wang, Z. Xie, Y. Wang, Y. Ding, M.K.H. Leung, Y.H. Ng, Adv. Sci. 2024, DOI: 10.1002/advs.202402471.

51. N. Han, Y. Wang, B-L. Su, Unveiling oscillatory nature for sustainable fuel production, Natl. Sci. Rev. 5 (2024) nwae068.

52. N. Han, W. Zhang, W. Guo, H. Pan, B. Jiang, L. Xing, H. Tian, G. Wang, X. Zhang, J. Fransaer, Designing Oxide Catalysts for Oxygen Electrocatalysis: Insights from Mechanism to Application, Nano-Micro Lett. 15 (2023) 185.